Journal of Sound and Vibration 330 (2011) 2536–2553

Contents lists available at ScienceDirect

Journal of Sound and Vibration

journal homepage: www.elsevier.com/locate/jsvi

Wave propagation characterization and design of two-dimensional elastic chiral metacomposite

X.N. Liu [a,b], G.K. Hu [b], C.T. Sun [c], G.L. Huang [a,*]

[a] Department of Systems Engineering, University of Arkansas at Little Rock, Little Rock, AR 72204, USA
[b] School of Aerospace Engineering, Beijing Institute of Technology, Beijing 100081, China
[c] School of Aeronautics and Astronautics, Purdue University, West Lafayette, IN 47907, USA

A R T I C L E I N F O

Article history:
Received 17 August 2010
Received in revised form
1 December 2010
Accepted 16 December 2010
Handling Editor: G. Degrande
Available online 19 January 2011

A B S T R A C T

In this work, a chiral metacomposite is proposed by integrating two-dimensional periodic chiral lattice with elastic metamaterial inclusions for low-frequency wave applications. The plane harmonic wave propagation in the proposed metacomposite is investigated through the finite element technique and Bloch's theorem. Band diagrams are obtained to illustrate wave properties of the chiral metacomposite. Effective dynamic properties of the chiral metacomposite are numerically calculated to explain low-frequency bandgap behavior in the chiral metacomposite. Interestingly doubly negative effective density and modulus of the chiral metacomposite are found in a specific frequency range, where a pass band with negative group velocity is observed. Tuning of the resulting low-frequency bandgaps is then discussed by adjusting microstructure parameters of the metamaterial inclusion and lattice geometry. Specifically design of a metacomposite beam structure for the broadband low-frequency vibration suppression is demonstrated.

1. Introduction

Lattice structures are used widely in a variety of engineering applications due to their outstanding stiffness-to-weight ratio and high designable features. Typical engineering applications of lattice structures include space trusses [1] and sandwich beams and panels [2]. Many lattice structures of various topologies have been proposed and extensively investigated. Among these structures, chiral topologies [3], which have distinctive mechanical properties such as high shear rigidity and negative Poisson's ratio, are regarded as a superior choice for different engineering applications [4]. The static behavior of the lattice/cellular solids has been intensively studied and fruitful results were found [5–7].

In the same time, wave propagation in periodic lattice materials has also drawn much attention. Both physicists and structural engineers [8–10] found that wave propagation in periodic structures exhibits characteristic pass and stop bands. Many efforts have been made to tailor lattice structures to achieve desired bandgap characteristics such that wave propagation is forbidden in a specified frequency regime. A systematic study based on topology optimization procedures was conducted to design phononic crystals with optimized bandgap properties [11,12]. The in-plane elastic wave propagation in four representative planar lattice topologies: hexagonal, Kagomé, triangular and square honeycomb were simulated to examine wave bandgaps and spatial filtering phenomena [13]. Wave directional behavior in cellular lattices

* Corresponding author. Tel.: +1 501 683 7522; fax: +1 501 569 8698.
E-mail address: glhuang@ualr.edu (G.L. Huang).

0022-460X/$ - see front matter
doi:10.1016/j.jsv.2010.12.014

and occurrence of wave beaming at specified frequencies were also investigated [14]. Phononic properties of the chiral lattice were recently examined [15]. However, it is well known that the phononic bandgaps in most periodic lattice structures are mostly limited in mid-high frequency ranges. This is because wave mechanism in the bandgaps is due to the Bragg scattering, which requires that the microstructure size must be comparable to the corresponding wavelength. There are great needs to design lattice structures with low-frequency bandgaps for engineering applications.

To enhance low-frequency wave suppression of lattice structures, most common methods are add-on treatments by adding different microstructure or materials into the structures. Martinsson and Movchan [16] demonstrated that a microstructure of concentrated masses connected to the primary lattice structure by a soft link can result in low-frequency bandgaps. Introduction of resonating microstructures into the lattice structure is now considered as one of the most efficient approaches for the low-frequency bandgaps. Many similar approaches based on the added resonance mechanism can be found recently [17,18]. Following this concept, metamaterials, which are the materials with elaborately tailored microstructures, will be an excellent candidate for this purpose. From the wave mechanism point of view, metamaterials are composites whose building block can exhibit resonance under wave excitation. This concept was first introduced in 1968 by Soviet physicist Veselago [19] for eletromagnetics (EM), and the proof-of-concept prototype of the EM metamaterial was realized in 2000 [20]. Inspired by the EM wave, metamaterials are extended in parallel to elastic and acoustic (EA) waves based on the similarity between the EM wave and the EA wave. Liu et al. [21] fabricated and investigated a metamaterial based on the idea of localized resonant structures that exhibit bandgaps with a lattice constant two orders of magnitude smaller than the relevant wavelength. This idea had given a possible solution to the length-scale problem of bandgap materials. The realization of robust elastic wave bandgaps in the low-frequency range can be clearly explained by the negative effective mass density [22] of the metamaterial within certain frequency range. Li and Chan [23] reported theoretically a possibility of the existence of acoustic/elastic metamaterials. They utilized the effective mass density and bulk modulus derived by Berryman [24] and showed that both the effective mass density and bulk modulus can be simultaneously negative, in the sense of an effective medium. They claimed that the double negativity is derived from low-frequency resonances, as in the case of electromagnetism, but the negative density and modulus are derived from a single resonance structure as distinct from electromagnetism in which the negative permeability and negative permittivity originates from different resonance mechanisms.

In the paper, we propose a new chiral metacomposite for the low-frequency bandgaps and wave filtering application. The metacomposite is composed of a two dimensional periodic chiral lattice and a typical metamaterial inclusion. The metamaterial inclusion is composed of a softly coated heavy cylinder, as proposed by Liu et al. [21]. The in-plane free wave motion in the metacomposite is investigated through the finite element technique and Bloch's theorem. Effective dynamic properties of the chiral metacomposite are numerically determined in the low frequency range. Doubly negative effective mass density and modulus are found at a specific frequency range, where a pass band with negative group velocity is observed. Tuning of the low-frequency bandgaps is also revealed by adjusting microstructure parameters of the metacomposite. Specifically design of a metacomposite beam for broadband wave filtering application is suggested.

The present paper is organized into five sections including Section 1—Introduction. Section 2 presents the geometry of the proposed chiral lattice metacomposite. Section 3 describes the numerical method for the study of its characteristic wave behavior. Section 4 discusses the relative numerical results. Finally the concluding remarks is summarized in Section 5.

2. Geometries of the chiral metacomposite

In the study, a chiral metacomposite is proposed by integrating a two-dimensional chiral lattice with a metamaterial inclusion as low-frequency resonators. The topology of the hexagonal chiral lattice [3] is shown in Fig. 1a. The structural layout is defined by circles of equal radius r linked by straight ligaments of equal length L. The ligaments are required to be tangential to the circles and the angle between adjacent ligaments is equal to sixty degrees. The distance between circle centers is denoted as R, while the angle between the line connecting the circle centers and the ligaments is defined as β. The wall thickness of circles and ligaments are denoted as t_c and t_b, respectively. Based on Fig. 1a, we have

$$\sin\beta = \frac{2r}{R}, \quad \cos\beta = \frac{L}{R} \tag{1}$$

Among the parameters, the ratio L/R is of importance and denoted as the topology parameter [15]. The lattice is in-plane isotropic and its Poisson's ratio is around -1. To obtain low-frequency stop bands, a metamateraial inclusion, a softly coated heavy cylinder (or disk), is added in the circles, as shown in Fig. 1b. Radius of the core cylinder is denoted as r_c.

The whole chiral metacomposite assembly can be obtained by tessellating a unit cell on the sites determined by all linear combination of the lattice vectors $n_1\mathbf{e}_1+n_2\mathbf{e}_2$, as shown in Fig. 2a, where n_i are integers and $\mathbf{e}_i$ are basic lattice vectors with $i=1,2$. The basic lattice vectors $\mathbf{e}_i$ can be written in the orthogonal Cartesian vector basis $(\mathbf{i}_1,\mathbf{i}_2)$ as

$$\begin{aligned}\mathbf{e}_1 &= (\sqrt{3}\mathbf{i}_1+\mathbf{i}_2)R/2\\ \mathbf{e}_2 &= (-\sqrt{3}\mathbf{i}_1+\mathbf{i}_2)R/2\end{aligned} \tag{2}$$

Due to the periodicity, location of a point P in cell (n_1,n_2) can be expressed as

$$\mathbf{r}_P(n_1,n_2) = \hat{\mathbf{r}}_P + n_1\mathbf{e}_1 + n_2\mathbf{e}_2 \tag{3}$$

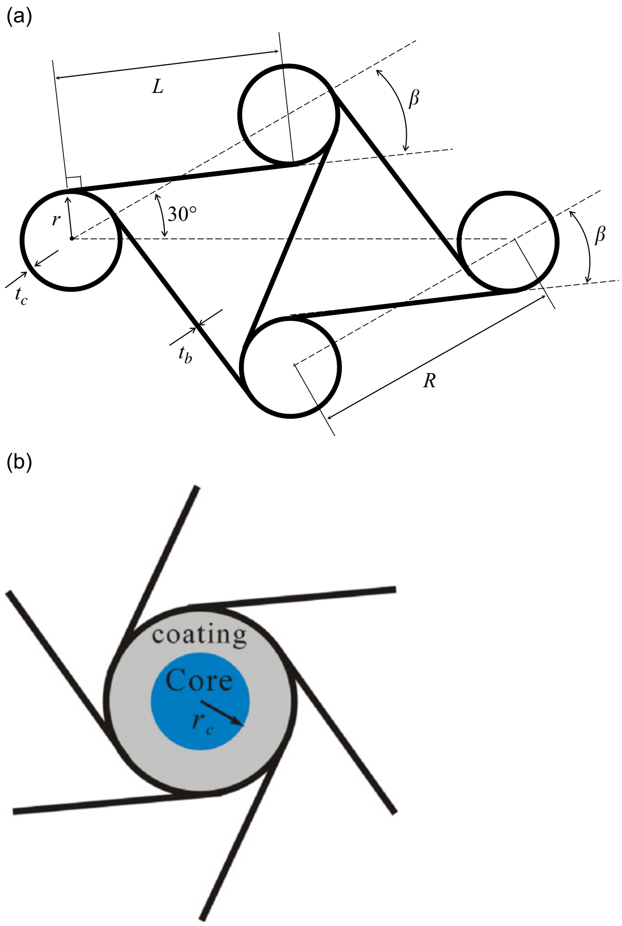

Fig. 1. (a) Geometry of a hexagonal chiral lattice and (b) unit cell of the chiral metacomposite.

where $\hat{\mathbf{r}}_P$ defines position of the point corresponding to P in the reference cell (0,0). Given the direct lattice space defined by the basic lattice vectors, basic reciprocal lattice vectors ($\mathbf{b}_1$,$\mathbf{b}_2$), as shown in Fig. 2b, can be defined as

$$\mathbf{b}_i \cdot \mathbf{e}_j = 2\pi\delta_{ij} \tag{4}$$

where δ_{ij} is the Kronecker delta. For the present chiral assembly, we have

$$\mathbf{b}_1 = \frac{2\pi}{R}\left(\frac{\mathbf{i}_1}{\sqrt{3}}+\mathbf{i}_2\right), \quad \mathbf{b}_2 = \frac{2\pi}{R}\left(-\frac{\mathbf{i}_1}{\sqrt{3}}+\mathbf{i}_2\right) \tag{5}$$

3. Finite element procedure of free wave motion

The elastic wave propagation in a periodic structure is characterized by Bloch's theorem [8]. If a harmonic plane wave is admitted, the displacement $\mathbf{u}$ at a point P in the reference unit cell can be expressed as

$$\mathbf{u}(\hat{\mathbf{r}}_P) = \mathbf{u}_P e^{i(\omega t - \mathbf{k}\cdot\hat{\mathbf{r}}_P)} \tag{6}$$

where $\mathbf{u}_P$ is the wave amplitude, ω is the angular frequency and $\mathbf{k}$ is the wave vector and $i=\sqrt{-1}$. According to Bloch's theorem, displacement of the point corresponding to Pat location $\mathbf{r}_P(n_1,n_2)$can be written in terms of the displacement of the reference unit cell as follows:

$$\mathbf{u}(\mathbf{r}_P) = \mathbf{u}(\hat{\mathbf{r}}_P)e^{i\mathbf{k}\cdot(\mathbf{r}_P-\hat{\mathbf{r}}_P)} = \mathbf{u}(\hat{\mathbf{r}}_P)e^{i(n_1k_1+n_2k_2)} \tag{7}$$

where $k_i = \mathbf{k}\cdot\mathbf{e}_i$ with $i=1,2$. Bloch's theorem, as described by Eq. (7), states that for any structure with repetitive identical unit cells, changes in complex wave amplitude from cell to cell, due to a propagating wave without attenuation, do not depend on the cell location within the periodic system. By virtue of the theorem, wave propagation in the entire lattice can be fully identified by wave motion within the reference unit cell.

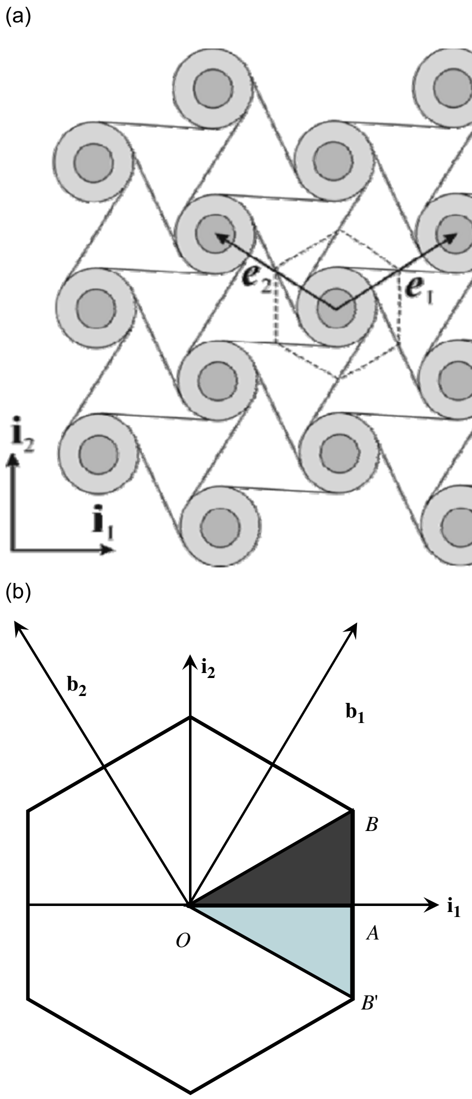

Fig. 2. (a) Lattice layout and lattice vector and (b) reciprocal lattice and Brillouin zone.

While the direct lattice defines spatial periodicity of the considered domain, the reciprocal lattice describes the periodicity of the frequency-wave vector relation. According to Eq. (4), the wave vector $\mathbf{k}$ can be expressed as $\mathbf{k}=k_1\mathbf{b}_1+k_2\mathbf{b}_2$. If we replace $\mathbf{k}$ by $\mathbf{k}'=\mathbf{k}+m_1\mathbf{b}_1+m_2\mathbf{b}_2$ in Eq. (7), then the following relation is obtained as

$$\mathbf{u}(\mathbf{r}_P)=\mathbf{u}(\hat{\mathbf{r}}_P)e^{i(n_1k_1{}'+n_2k_2{}')},\quad k_i'=\mathbf{k}'\cdot\mathbf{e}_i=k_i+2\pi m_i \tag{8}$$

which indicates the periodicity of the wave vector. In the two-dimensional lattice, the period corresponds to a region in the reciprocal lattice whose area equals the area of the reciprocal lattice's unit cell, known as the first Brillouin zone, as shown in Fig. 2b. For the traditional hexagonal lattice, dark sub-region OAB in Fig. 2b is identified as the Irreducible Brillouin Zone (IBZ), which is the smallest frequency-wave vector space to determine wave dispersion. The Brillouin zone points are shown in Table 1. The wave vectors are chosen along the locus OAB; i.e., along the edges of the irreducible part of the first Brillouin zone. For the traditional hexagonal lattice, instead of covering the entire IBZ, it is sufficient for $\mathbf{k}$ along its feature path OABO in Fig. 2b. However, for the chiral structure, reflective symmetry may not be applicable and the path BB′ in Fig. 2b should be considered.

The free wave propagation in the infinite lattice can be studied by solving the elastodynamics on the unit cell and Bloch's theorem. Due to geometric complexity of the current structure, the finite element (FE) technique is employed. The FE discretization of the unit cell is shown in Fig. 3, where the circle and ligaments of the chiral lattice are discretized by Timoshenko beam elements, while the metamaterial inclusion is modeled by four-node plane solid elements. Application

Table 1
The irreducible Brillouin zone points of the lattice.

	Cartesian basis	Reciprocal basis
O	(0,0)	(0,0)
A	$\left(\frac{2\pi}{\sqrt{3}R},0\right)$	$\left(\frac{1}{2},-\frac{1}{2}\right)$
B	$\left(\frac{2\pi}{R\sqrt{3}},\frac{2\pi}{3R}\right)$	$\left(\frac{2}{3},-\frac{1}{3}\right)$

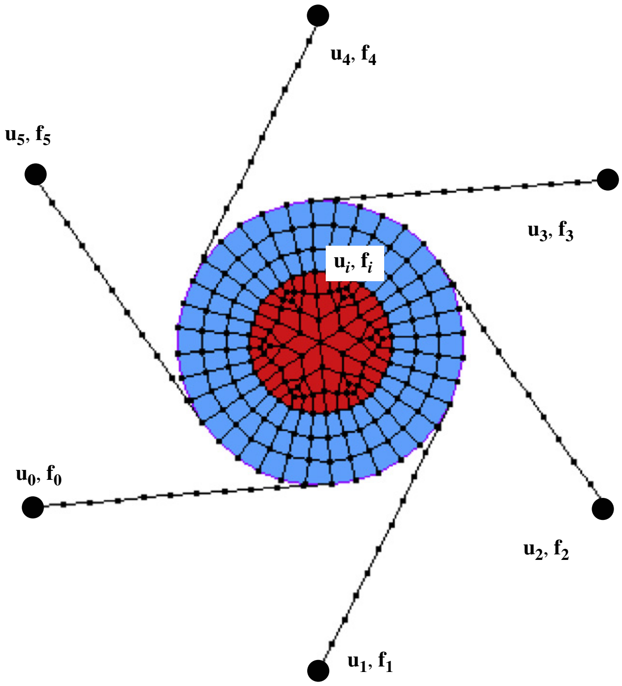

Fig. 3. Finite element discretization of the unit cell.

of standard FE procedures [25] yields the unit cell's discretized equation of motion in the following matrix form:

$$(\mathbf{K}-\omega^2\mathbf{M})\mathbf{u} = \mathrm{D}\mathbf{u} = \mathbf{f} \tag{9}$$

where **K** and **M** are the global mass and stiffness matrices, **u** and **f** are the vectors of generalized nodal displacements and forces, respectively, $\mathbf{D}=(\mathbf{K}-\omega^2\mathbf{M})$ is the dynamic stiffness.

For convenience, the vectors containing generalized nodal displacements **u** and forces **f** in the cell are defined in the form [15]

$$\mathbf{u} = \left\{ \mathbf{u}_0 \quad \mathbf{u}_1 \quad \mathbf{u}_2 \quad \mathbf{u}_3 \quad \mathbf{u}_4 \quad \mathbf{u}_5 \quad \mathbf{u}_i \right\}^T$$
$$\mathbf{f} = \left\{ \mathbf{f}_0 \quad \mathbf{f}_1 \quad \mathbf{f}_2 \quad \mathbf{f}_3 \quad \mathbf{f}_4 \quad \mathbf{f}_5 \quad \mathbf{f}_i \right\}^T \tag{10}$$

where subscripts 0–5 identify quantities belongs to six boundary nodes, subscript $i$denotes quantities of internal nodes, which are highlighted in Fig. 3. By virtue of Bloch's theorem, we have

$$\mathbf{u}_3 = \mathbf{u}_0 e^{ik_1}, \quad \mathbf{u}_4 = \mathbf{u}_1 e^{i(k_1+k_2)}, \quad \mathbf{u}_5 = \mathbf{u}_2 e^{ik_2} \tag{11a}$$

$$\mathbf{f}_3 = -\mathbf{f}_0 e^{ik_1}, \quad \mathbf{f}_4 = -\mathbf{f}_1 e^{i(k_1+k_2)}, \quad \mathbf{f}_5 = -\mathbf{f}_2 e^{ik_2} \tag{11b}$$

Eqs. (9) and (11) constitute a FE problem with constraint conditions in complex form. Most standard FE software does not have features to directly deal with the problem with complex variables. In the study, the difficulty is overcome by solving problems with real and imaginary parts of the constraint conditions separately. Considering the problem with two identical meshes, the field equation including the real and imaginary parts can be written as

$$\begin{bmatrix} \mathbf{D} & 0 \\ 0 & \mathbf{D} \end{bmatrix} \begin{Bmatrix} \mathbf{u}^{\mathrm{Re}} \\ \mathbf{u}^{\mathrm{Im}} \end{Bmatrix} = \begin{Bmatrix} \mathbf{f}^{\mathrm{Re}} \\ \mathbf{f}^{\mathrm{Im}} \end{Bmatrix} \tag{12}$$

where superscripts ‘Re’ and ‘Im’ denote real and imaginary parts of the fields in Eq. (10). The real and imaginary parts communicate on their boundary nodes through the constraint Eq. (11a). For example, displacements of nodes 0 and 3 can be written as

$$\begin{aligned} \mathbf{u}_3^{\mathrm{Re}} &= \mathbf{u}_0^{\mathrm{Re}} \cos k_1 - \mathbf{u}_0^{\mathrm{Im}} \sin k_1 \\ \mathbf{u}_3^{\mathrm{Im}} &= \mathbf{u}_0^{\mathrm{Re}} \sin k_1 + \mathbf{u}_0^{\mathrm{Im}} \cos k_1 \end{aligned} \tag{13}$$

Eq. (11a) can be rewritten in matrix form as

$$\begin{Bmatrix} \mathbf{u}^{\mathrm{Re}} \\ \mathbf{u}^{\mathrm{Im}} \end{Bmatrix} = \mathbf{Q} \begin{Bmatrix} \mathbf{u}_r^{\mathrm{Re}} \\ \mathbf{u}_r^{\mathrm{Im}} \end{Bmatrix} \tag{14}$$

where the subscript r represents the reduced vector $\mathbf{u}_r^{\mathrm{Re}} = \begin{Bmatrix} \mathbf{u}_0^{\mathrm{Re}} & \mathbf{u}_1^{\mathrm{Re}} & \mathbf{u}_2^{\mathrm{Re}} & \mathbf{u}_i^{\mathrm{Re}} \end{Bmatrix}^T$, and $\mathbf{Q}$ is the corresponding rectangular matrix. Substituting Eq. (14) into (12) and premultiplying by $\mathbf{Q}^T$ yield the reduced field equation

$$\mathbf{Q}^T \begin{bmatrix} \mathbf{D} & 0 \\ 0 & \mathbf{D} \end{bmatrix} \mathbf{Q} \begin{Bmatrix} \mathbf{u}_r^{\mathrm{Re}} \\ \mathbf{u}_r^{\mathrm{Im}} \end{Bmatrix} = \begin{Bmatrix} \mathbf{f}_r^{\mathrm{Re}} \\ \mathbf{f}_r^{\mathrm{Re}} \end{Bmatrix} \quad \text{or} \quad \tilde{\mathbf{D}}\tilde{\mathbf{u}} = \tilde{\mathbf{f}} \tag{15}$$

The eigenvalue problem $\tilde{\mathbf{D}}(\mathbf{k},\omega)\tilde{\mathbf{u}} = 0$ of Eq. (15) is solved by a standard FE software to obtain dispersion curves of the structure. In the study, the problem is solved by a commercial FE package ANSYS. The complete surface $\omega = \omega(\mathbf{k})$ is denoted as phase constant surface or dispersion surface. There exist as many surfaces as there are eigenvalues of the problem. If two surfaces do not overlap each other, there exists a wave bandgap in which no wave propagation occurs. Furthermore, the normal to the phase constant surface at any point gives the Poynting vector or group velocity, and this indicates the speed and direction of energy flow.

4. Numerical simulation

In this section, wave propagation of the proposed metacomposite structure is numerically studied. The free wave motion properties are reported in the form of band diagrams, dispersion surfaces as well as phase and group speeds. Effective properties of the proposed structure are also determined to further explain the low-frequency bandgap behavior. Numerical simulation is also conducted to study microstructure effects on the wave propagation characteristics. Finally design of a finite metacomposite beam structure is suggested and demonstrated for the low-frequency wave filtering application. In the following, results are presented in normalized frequency $\Omega = \omega/\omega_0$ with $\omega_0 = \pi^2\sqrt{(E_l t_b^2)/(12\rho_l L^4)}$, which is the first flexural frequency of a simply supported ligament of length L. A reference configuration of the structure, including geometry and material parameters, is shown in Table 2.

4.1. Band diagrams

To explore the bandgap behavior, band diagram of the structure is constructed where the normalized wave frequency Ω is plotted against the wave vector $\mathbf{k}$. In the study, the path OABO in Fig. 2b is considered because it gives sufficient accuracy for the wave characteristics of the structure, which is also reflected from the dispersive surfaces in the next section.

First, a modal analysis is conducted to understand effects of the metamaterial inclusion. Fig. 4 shows the first three typical eigenmodes and their corresponding frequencies. In the simulation, boundary of the metamaterial inclusion is fixed. It can be found that the first two basic resonance modes are caused by rigid translation and rotation of the core in the soft coating layer

Table 2
Geometric and material parameters of reference configuration.

Lattice parameters		Metamaterial parameters	
Topology parameter	$L/R = 0.9$	Core to node ratio	$r_c/r = 0.5$
Ligament length	$L/R = 26.4\,\mathrm{mm}$	Young’s modulus of core	$E_c = 17\,\mathrm{GPa}$
Node radius	$r = 6.4\,\mathrm{mm}$	Poisson’s ratio of core	$\nu_c = 0.33$
Ligament wall thickness	$t_b = 0.5\,\mathrm{mm}$	Density of core	$\rho_c = 13\,\mathrm{g/cm^3}$
Node wall thickness	$t_c = 0.5\,\mathrm{mm}$	Young’s modulus of coating	$E_s = 5\,\mathrm{MPa}$
Young’s modulus	$E_l = 71\,\mathrm{GPa}$	Poisson’s ratio of coating	$\nu_s = 0.33$
Poisson’s ratio	$\nu_l = 0.33$	Density of coating	$\rho_s = 0.5\,\mathrm{g/cm^3}$
Density	$\rho_l = 2.7\,\mathrm{g/cm^3}$		

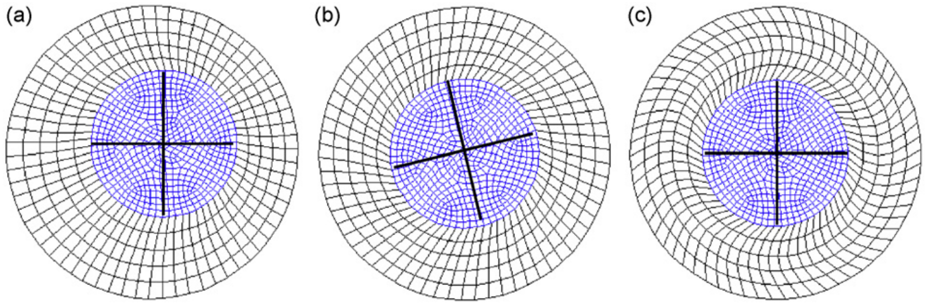

Fig. 4. The first three eigenmodes of the metamaterial inclusion: (a) $\Omega = 0.83$; (b) $\Omega = 1.15$ and (c) $\Omega = 6.04$.

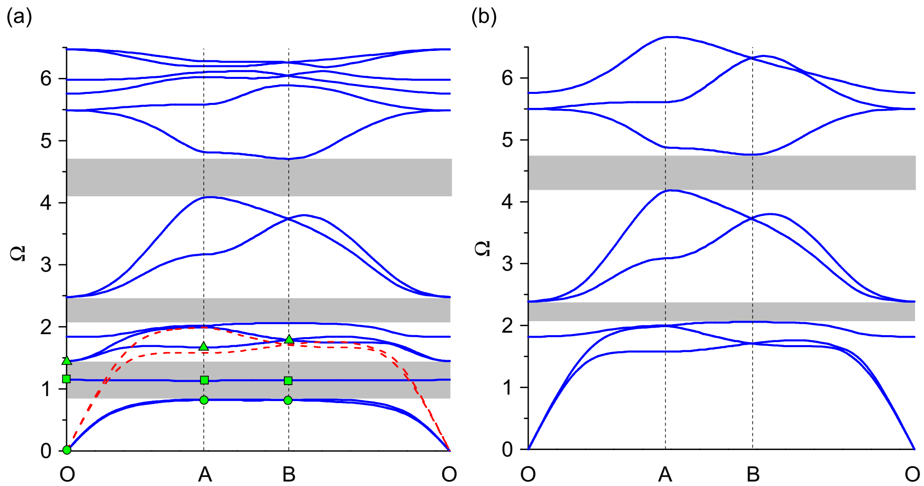

Fig. 5. Band diagrams of the lattice (a) with metamaterial inclusions and (b) without metamaterial inclusions (for interpretation of the references to color in this figure, the reader is referred to the web version of this article).

(Fig. 4a and b); however, the third resonance mode is caused by the local deformation in the coating layer (Fig. 4c). The band diagram of the metacomposite is shown in Fig. 5a. For reference, the band diagram of the lattice structure without the metamaterial inclusion is also plotted in Fig. 5b. From the comparison in Fig. 5a and b, it can be immediately revealed that the metamaterial inclusion has significant effects on the wave behavior of the structure, especially at the low-frequency range. A low-frequency bandgap in the range [0.81, 1.43] appears, which is absent in the pure chiral lattice. The frequency range of the low-frequency bandgap is close to the first and second resonant modes of the metamaterial inclusion at Ω=0.83 and 1.15 (Fig. 4a), which indicates formation of the low-frequency bandgap is due to the local resonance of the metamaterial inclusion. For clear demonstration, dispersion curves of the first two lowest modes of the lattice without the metamaterial inclusion in Fig. 5b are also added in Fig. 5a by red dashed lines, which correspond the P (longitudinal) and S (transverse) wave modes. From the comparison, it can be found that the first two lowest wave branches of the original lattice structure are separated into five branches due to the local resonance of the metamaterial inclusion. It is also noticed that band structures in the two lattice structures with and without the metamaterial inclusion are almost unchanged at frequency range $\Omega \in [2,6]$. This 'uncoupled' feature is of great advantage for the design and optimization procedure to yield desired stop bands.

Another interesting feature in Fig. 5a is the almost flat third branch which implies that its wave group velocity is close to zero. Though narrow, this is indeed a pass band in $\Omega = [1.14, 1.16]$ interval. Specifically the negative slope along the OA path is observed in the pass band, which implies appearance of a negative group velocity in the low-frequency range. The negative slope becomes more obvious with increase of the microstructure geometry ratio r_c/r. The negative group velocity in a low-frequency range and the related concept of negative refraction index are the striking phenomena in the so-called *left handed materials* (*LHM*), which have simultaneously negative effective density and modulus in elastic media [23]. Many efforts have been undertaken in this subject, however, to our best knowledge, there is no practicable elastic LHM proposed in solid materials. In the study, the rigid translational resonance of the core may induce negative effective density of the composite, our preliminary results show that the rigid rotational resonance together with the ligament may provoke negative effective modulus.

Another attempt to explain the formation of the new low-frequency bandgaps can be made through the analysis of the associated wave modes. Fig. 6 shows mode shapes of the first, third and fourth dispersive branches located at the points (O, A, B) of the IBZ, respectively, which are shown in Fig. 5a. In Fig. 6, undeformed geometry (red line) is imposed as

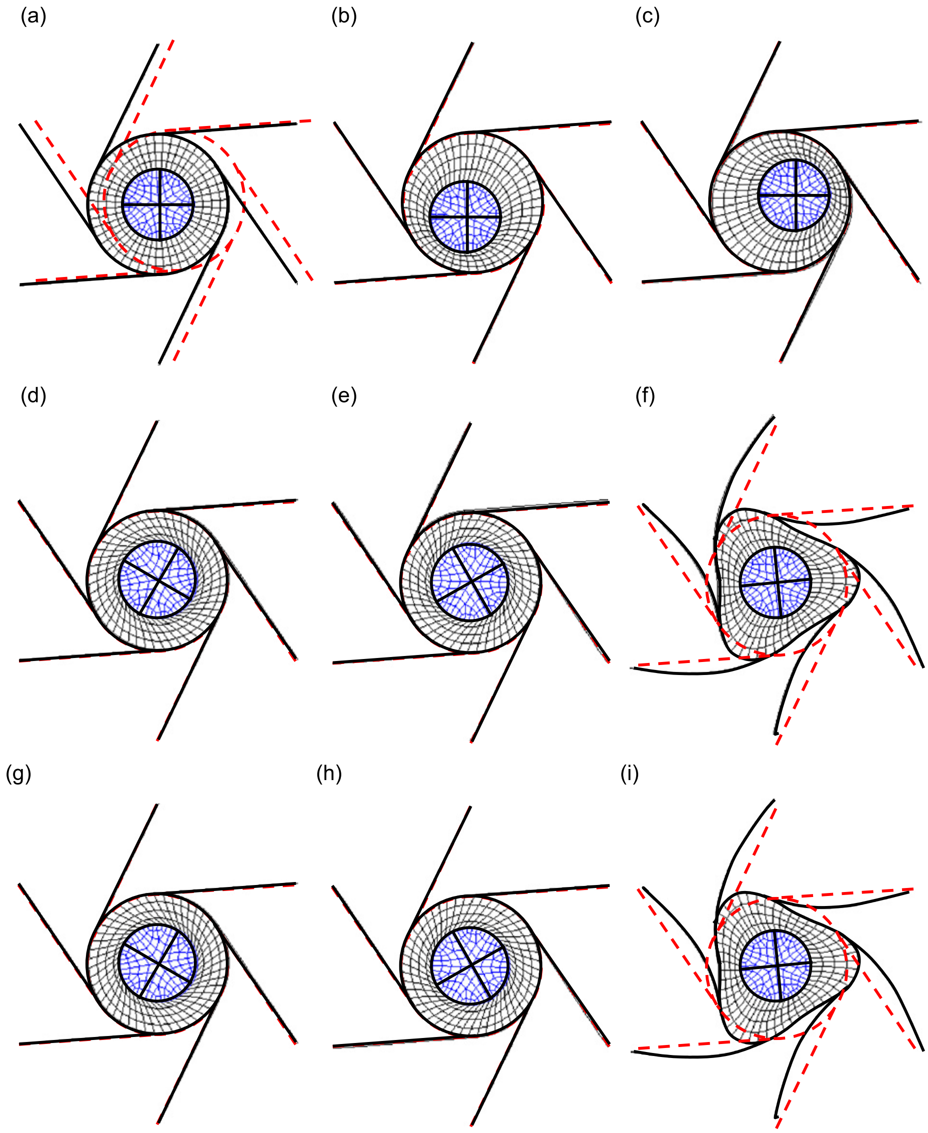

Fig. 6. Mode shapes for reference configuration: (a–c) 1st branch; (d–f) 3rd branch and (g–i) 4th branch (for interpretation of the references to color in this figure, the reader is referred to the web version of this article).

reference. Fig. 6a–c shows wave modes of the first dispersive branch at points O, A, B, which are highlighted by green circles in Fig. 5a. Mode shape in Fig. 6a corresponds to the rigid-motion of the whole structure, while the mode shapes in Fig. 6b and c illustrate that main deformation of the structure is a rigid translation of the core in the soft coating layer and the lattice structure is almost undeformed. In this case, most wave energies are trapped in the metamaterial inclusion due to its local resonance. Fig. 6d, e, f shows wave modes of the third dispersive branch at points O, A, B, respectively, which are highlighted by green triangles in Fig. 5a. Mode shape at point O is associated with the second rotational resonance of the metamaterial inclusion. From the mode shapes at points A and B, it can be found that the wave motion of the structure is mainly through the rotation resonance of the core and rib around the second natural frequency Ω=1.15 of the metamaterial inclusion. Fig. 6g, h, i shows wave modes of the fourth dispersive branch at points O, A, B, respectively, which are highlighted by green squares in Fig. 5a. Mode shape at point O is related to the first resonance of the core of the metamaterial inclusion. Mode shapes at points A and B show how propagation of the polarizations occurs mostly through the bending deformation of the lattice ribs.

4.2. Effective properties of the chiral metacomposite

The use of dynamic effective mass density and modulus has proved successfully in describing and predicting wave propagation in elastic metamaterials [26]. In the section, dynamic effective mass density and elastic modulus of the chiral metacomposite are numerically determined under the low-frequency assumption, where wavelength in the host medium (pure lattice) is much larger than size of the unit cell of the chiral metacomposite. Six boundary nodes of the unit cell, as shown in Fig. 3, are assumed to be subjected to a global displacement $\mathbf{u}^b = \tilde{\mathbf{u}}^b e^{i\omega t}$. In the study, displacement phase difference among the six boundary nodes is ignored due to the long wavelength assumption. Therefore, the effective mass of the unit cell can be obtained numerically through the averaged reaction force in the six boundary nodes as

$$m_{\text{eff}}(\omega) = \frac{|\tilde{\mathbf{F}}|}{-\omega^2 |\tilde{\mathbf{u}}^b|} \tag{16}$$

where $\tilde{\mathbf{F}}$ is the obtained amplitude of averaged resultant force in the six boundary nodes of the unit cell. The effective mass density is taken as the volume average of the mass as

$$\rho_{\text{eff}} = m_{\text{eff}}/V_{\text{cell}} \quad \text{with} \quad V_{\text{cell}} = 3\sqrt{3}R^2/8 \tag{17}$$

where the thickness of the chiral metacomposite is assumed to be one.

The effective mass of the chiral metacomposite can also be estimated through a simple 'mass-in-mass' Lorentz model [27]. Based on the model, the effective mass of the chiral metacomposite can be written as

$$m_{\text{eff}} = m_1 + \frac{m_2\omega_0^2}{\omega_0^2 - \omega^2} \tag{18}$$

where m_1 and m_2 are the masses of the lattice frame and core, respectively, ω_0 is the local resonance frequency of the metamaterial inclusion, which can be numerically obtained as $\Omega_0 = 0.83$. Fig. 7 shows the normalized effective mass density of the chiral metacomposite in function of normalized wave frequency predicted by the proposed numerical method and the Lorentz model. In the figure, the normalized effective mass density of the chiral metacomposite is defined as $\rho^*_{\text{eff}} = \rho_{\text{eff}}/\rho_{\text{lattice}}$ with ρ_{lattice} being the density of the purely lattice structure. From the figure, very good agreement between the two methods is observed. It is also interesting to notice that the frequency range with the negative mass density matches the first bandgap in Fig. 5a quite well, which indicates that the wave mechanism in the first bandgap can be explained by out-of-phase effects between the momentum and velocity for the metamaterial inclusion.

To further explain the pass band with negative group velocity, as shown in Fig. 5, effective modulus of the chiral metacomposite should be determined. The major challenge of determination of effective modulus of the discrete lattice structure is how to apply the suitable displacement field to the discrete boundary nodes. In the study, the formulation of the continuum model with microstructures can be illustrated with the unit cell of a chiral metacomposite as shown in Fig. 8.

Using the classical micromechanics approach, the macro-strain and stress are defined, respectively, as the volume averages of the strain and stress fields in the representative volume element (RVE)

$$\mathbf{E} = \frac{1}{V}\int_V \boldsymbol{\varepsilon}\, dV = \langle \boldsymbol{\varepsilon} \rangle$$
$$\boldsymbol{\Sigma} = \frac{1}{V}\int_V \boldsymbol{\sigma}\, dV = \langle \boldsymbol{\sigma} \rangle \tag{19}$$

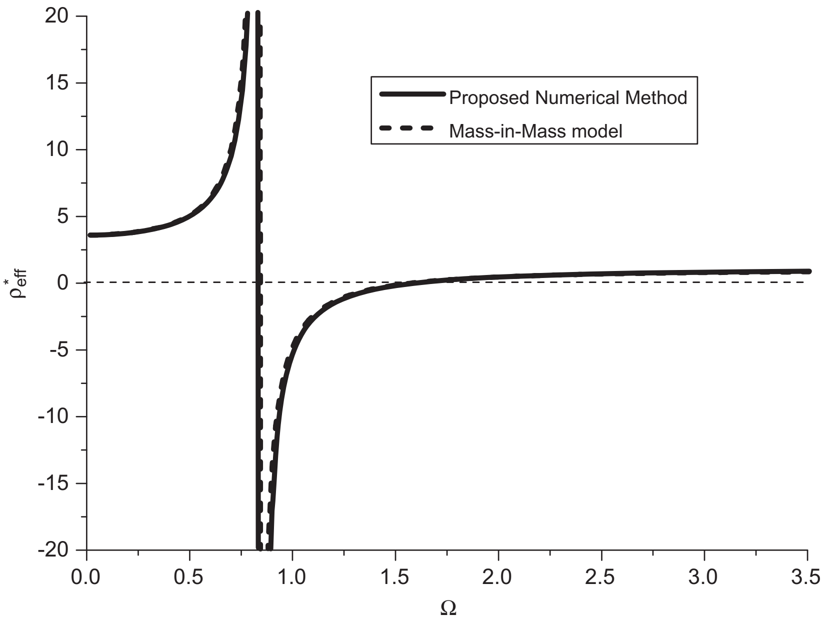

Fig. 7. Effective mass density of the chiral metacomposite.

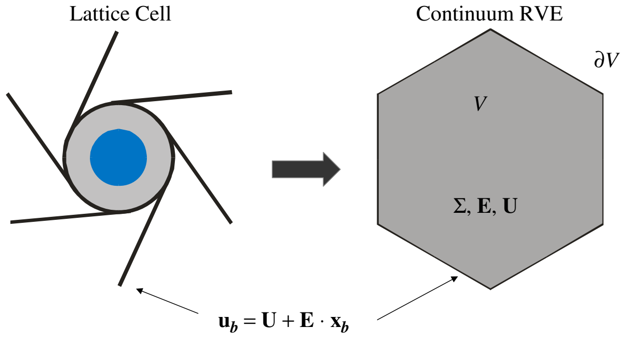

Fig. 8. Representation of a unit cell of a discrete chiral metacomposite by a homogeneous solid.

where $\boldsymbol{\sigma}$ and $\boldsymbol{\varepsilon}$ denote the local stress and strain fields in the original lattice medium, respectively, V is the volume of the RVE. Note that the macro displacement vector $\mathbf{U}$ is defined from the relation $\mathbf{E}=\frac{1}{2}(\nabla\otimes\mathbf{U}+\mathbf{U}\otimes\nabla)$.

Underlying the development of the continuum theory is the establishment of the relation between the local displacement field $\mathbf{u}$ and the macro-strain $\mathbf{E}$. In a RVE, the local displacement field, which is required to match the macro displacement at the boundary ∂V of the region occupied by the RVE, can be assumed as

$$\mathbf{u}^b=\mathbf{U}(\mathbf{X}_p)+\mathbf{E}\cdot\mathbf{x}^b \quad \text{at } \partial V \tag{20}$$

The above matching condition will be used for determination of the dynamic effective modulus of the discrete chiral metacomposite. To determine the effective bulk and shear modulus κ_{eff} and μ_{eff}, the global hydrostatic and pure shear deformation in the homogeneous continuum medium are considered by applying global strain field as

$$\mathbf{E}=\varepsilon\begin{bmatrix}1 & 0\\ 0 & 1\end{bmatrix} \quad \text{and} \quad \mathbf{E}=\varepsilon'\begin{bmatrix}1 & 0\\ 0 & -1\end{bmatrix} \tag{21}$$

where ε and ε' are the amplitudes of the applied strain field. For the unit cell of the discrete chrial metacomposite, the corresponding displacement for the hydrostatic and shear deformation can be applied to the six boundary nodes based on Eq. (20). The reaction forces at the boundary nodes are then calculated from the numerical analysis. The effective bulk modulus and shear modulus of the chiral metacomposite can be determined through the energy equivalence between the discrete unit cell and the homogenous continuum RVE as

$$W=\sum_{i=1}^{6}\mathbf{f}_i^b\cdot\mathbf{u}_i^b=4\kappa_{\mathrm{eff}}\varepsilon^2V$$
$$W=\sum_{i=1}^{6}\mathbf{f}_i^b\cdot\mathbf{u}_i^b=4\mu_{\mathrm{eff}}\varepsilon'^2V \tag{22}$$

respectively, where $\mathbf{f}_i^b$ are the calculated reaction forces at six boundary nodes.

Fig. 9 shows the normalized effective bulk modulus κ^*_{eff} and shear modulus μ^*_{eff} in function of the normalized frequency based on the proposed numerical method. The normalized effective elastic modulus is also plotted in the figure based on the relationship of $E^*_{\mathrm{eff}}=\kappa^*_{\mathrm{eff}}+\mu^*_{\mathrm{eff}}$ for the current two-dimensional problem. In the figure, the normalized effective parameters are defined as $\kappa^*_{\mathrm{eff}}=\kappa_{\mathrm{eff}}/\kappa^0_{\mathrm{eff}}$, $\mu^*_{\mathrm{eff}}=\mu_{\mathrm{eff}}/\kappa^0_{\mathrm{eff}}$ and $E^*_{\mathrm{eff}}=E_{\mathrm{eff}}/\kappa^0_{\mathrm{eff}}$ with κ^0_{eff} being the static effective bulk modulus. From Fig. 9, the effective negative bulk modulus is found in the frequency range $\Omega\in[1.05,1.17]$ and the effective negative elastic modulus is observed in the frequency range $\Omega\in[1.16,1.17]$, while the effective shear modulus is always positive. It is very interesting to notice that the common frequency range for both the effective negative mass density and effective negative modulus is found in the frequency range $\Omega\in[1.16,1.17]$, which is very close to that $\Omega\in[1.14,1.15]$ of the pass band with the negative group velocity. That means that the double negative properties of the chiral metacomposite are, at first time, achieved through combination of the chiral structure and the elastic metamaterial inclusion. The small shift about the frequency range with double negative properties may be attributed to the long wavelength assumption in the current model. Further correction incorporating the spatial dispersion effect and the chiral effect will be considered in the future.

4.3. Dispersion surfaces, phase and group speeds

In the section, free wave properties are presented and discussed by dispersion surfaces, phase and group velocities. Dispersion surfaces are evaluated in the entire Brillouin zone, and phase and group velocities provide important information about anisotropic wave behavior of the structure, which shows existence of preferential directions of propagation and energy flow.

Fig. 10 shows contours of dispersion surfaces of the first, fourth, eighth and ninth wave modes in the metacomposite. The first and fourth wave modes are lower and higher bands of the first low frequency bandgap. The contours are plotted in the first

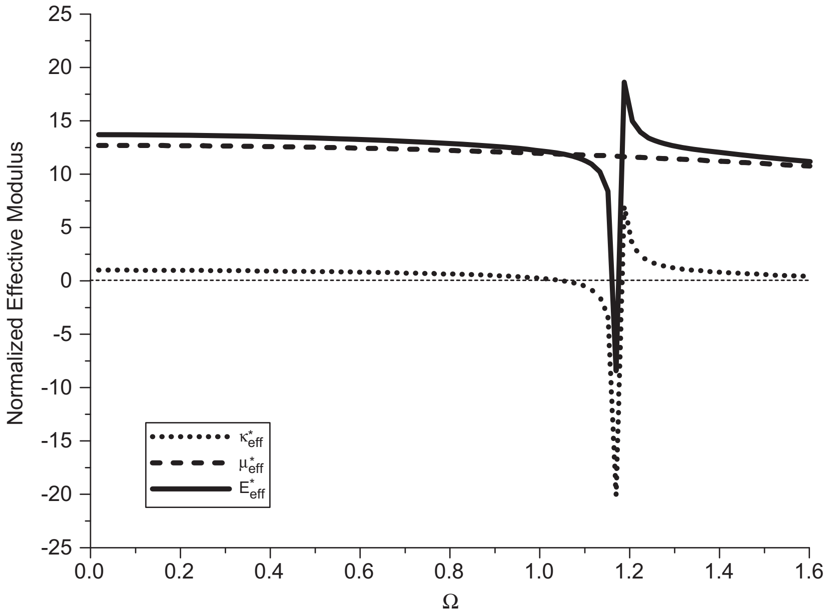

Fig. 9. Effective modulus of the chiral metacomposite.

Brillouin zone and in Cartesian space ($\mathbf{k}=\xi_1\mathbf{i}_1+\xi_2\mathbf{i}_2$). The IBZ is depicted in the figure by the dark triangle OAB. First, it can be found that the iso-frequency contours do not possess the reflective symmetry because of the chirality. The contour curves show isotropic when wave frequency is low, however, six-lobed contour curves become more apparent with the increase of wave frequency. In Fig. 10a, the dispersion surfaces change rapidly in low-frequency regime and become flat as the frequency reaches low bound of the first bandgap. This behavior is indicated by a large number of iso-frequency contour lines at short wave vectors and much lower contour density towards the edge of the first Brillouin zone. In Fig. 10b, contour lines of the fourth wave mode change rapidly at mediate wave vectors and become almost flat for small and large wave vectors. In Fig. 10c and d, it is interesting to observe that the shape of the contours change significantly with wave vectors, which is similar with the pure lattice. The wave propagation directionality is also clearly seen from Fig. 10. Isotropic behavior is found for the first and fourth wave modes for small magnitude of **k**, while anisotropic propagation behavior is found for other cases. This will be further clarified by the following phase and group velocity analysis.

Attention is also paid to wave phase and group velocities of the first and fourth wave modes. Specifically the phase velocity at a given frequency ω is evaluated by

$$\mathbf{c}_{\mathrm{ph}}=\frac{\omega}{k}\mathbf{k}_0 \tag{23}$$

where $k=|\mathbf{k}|o$ and $\mathbf{k}_0$ is a unit vector in the direction of the wave vector ($\mathbf{k}_0=\mathbf{k}/k$). Important indication regarding the energy flow within the metacomposite is represented by the group velocity as

$$\mathbf{c}_g=\frac{\partial\omega}{\partial\xi_1}\mathbf{i}_1+\frac{\partial\omega}{\partial\xi_2}\mathbf{i}_2 \tag{24}$$

The phase and group wave velocities are evaluated by variation of the wave vectors, i.e., the wave vectors change along the contour line at a desired frequency. Fig. 11a and c shows the normalized phase velocities in the first and fourth modes, respectively. In the figure, the phase velocity is plotted in the polar system, and velocity magnitudes are normalized by the phase velocity of the first wave mode at $\mathbf{k}=0$, which corresponds to the quasi-static case. At low-frequency cases, phase velocities are large in magnitude and the curve is approximately circular for both modes which implies nearly isotropic behavior. However, with the increase of wave frequency, the phase velocity decreases and wave propagation behavior becomes anisotropic.

Normalized group velocity dependence upon wave frequency in the first and fourth modes is shown in Fig. 11b and d, respectively. In the figure, velocity magnitudes are normalized by the phase velocity of the first wave mode at $\mathbf{k}=0$. In Fig. 11b, it can be found that the group velocity pattern in the first mode is similar to that of the phase velocity shown in Fig. 11a. The phase and group velocities are nearly identical at low frequencies, which further confirm the non-dispersive behavior for long wavelengths. As wave frequency increases, the group velocity becomes vanishing and anisotropy as the dispersive surface becomes flat. The anisotropic behavior of the fourth branch (Fig. 11d) displays a more complex pattern, which is characterized by caustics [15]. The caustics of group velocity plot corresponds the iso-frequency contour lines with alternative convex and concaves. Such caustics are associated with strong energy focusing along specific directions. To demonstrate phenomenon of the energy focusing, the fourth wave mode is shown in Fig. 12 at normalized frequency

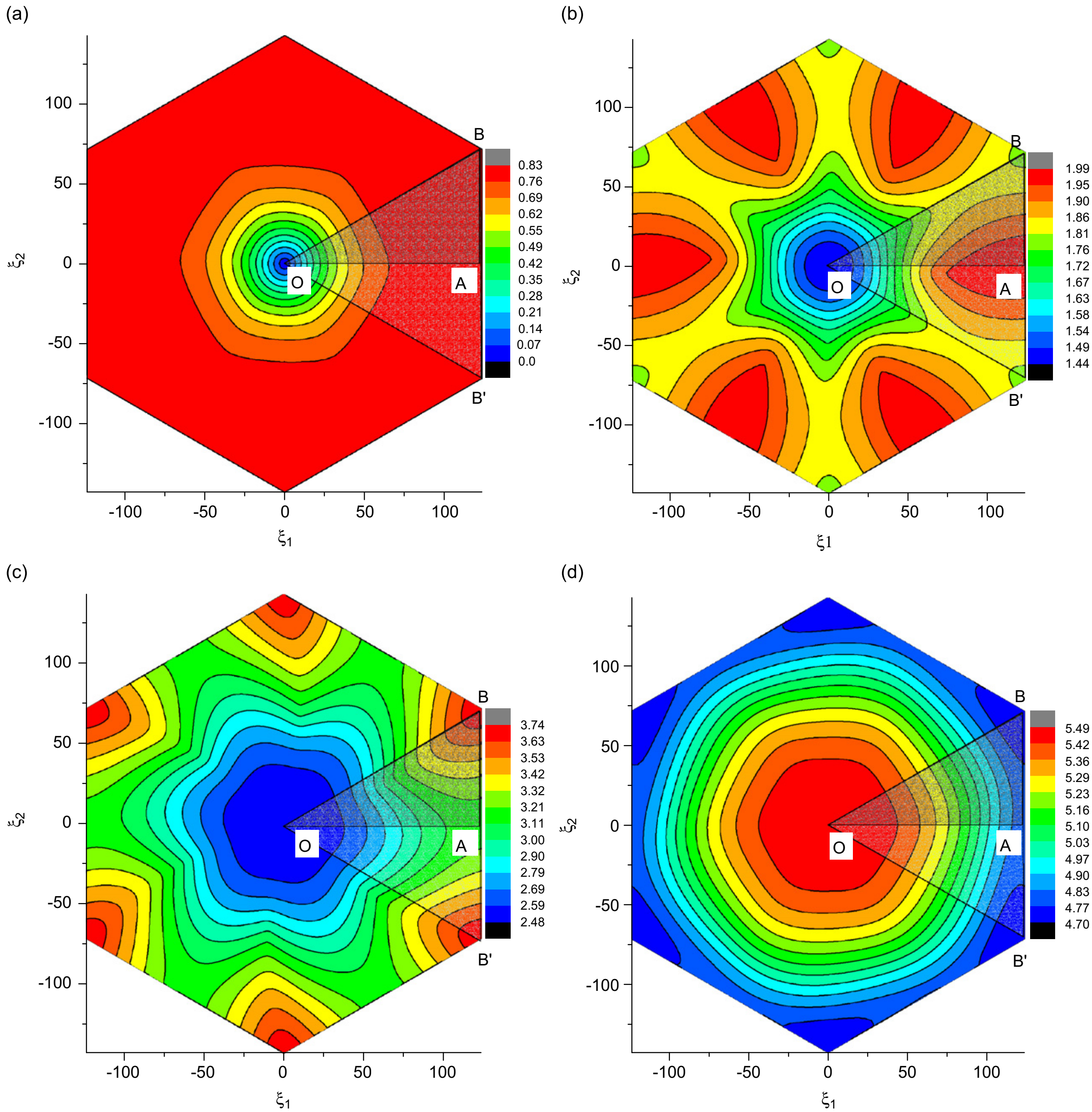

Fig. 10. Iso-frequency contours of (a) first mode, (b) fourth mode, (c) eighth mode and (d) ninth mode.

$\Omega = 1.75$, from which the wave front is presented. The topology parameters in Fig. 12 are the same as those in Fig. 11. The group velocity directions, which are normal to the wave front, appear to be mostly confined to four directions as shown in Fig. 12. If wave vectors spanning 360° is considered, the corresponding group velocity vectors are mostly oriented in six directions.

4.4. Microstructure effects on bandgaps of the chiral metacomposite

The objective of this section is to investigate microstructure effects on width and location of possible low-frequency bandgaps. Specifically effects of the topology parameters of the chiral lattice and microstructure configuration of the metamaterial inclusion upon the low-frequency bandgaps will be investigated.

Fig. 13 shows the band diagrams of the metacomposite structure for the topological parameters $L/R = 0.75$ and 0.6. In order to maintain the ligament length L unchanged, distance between the node centers R and node circle radius r varies

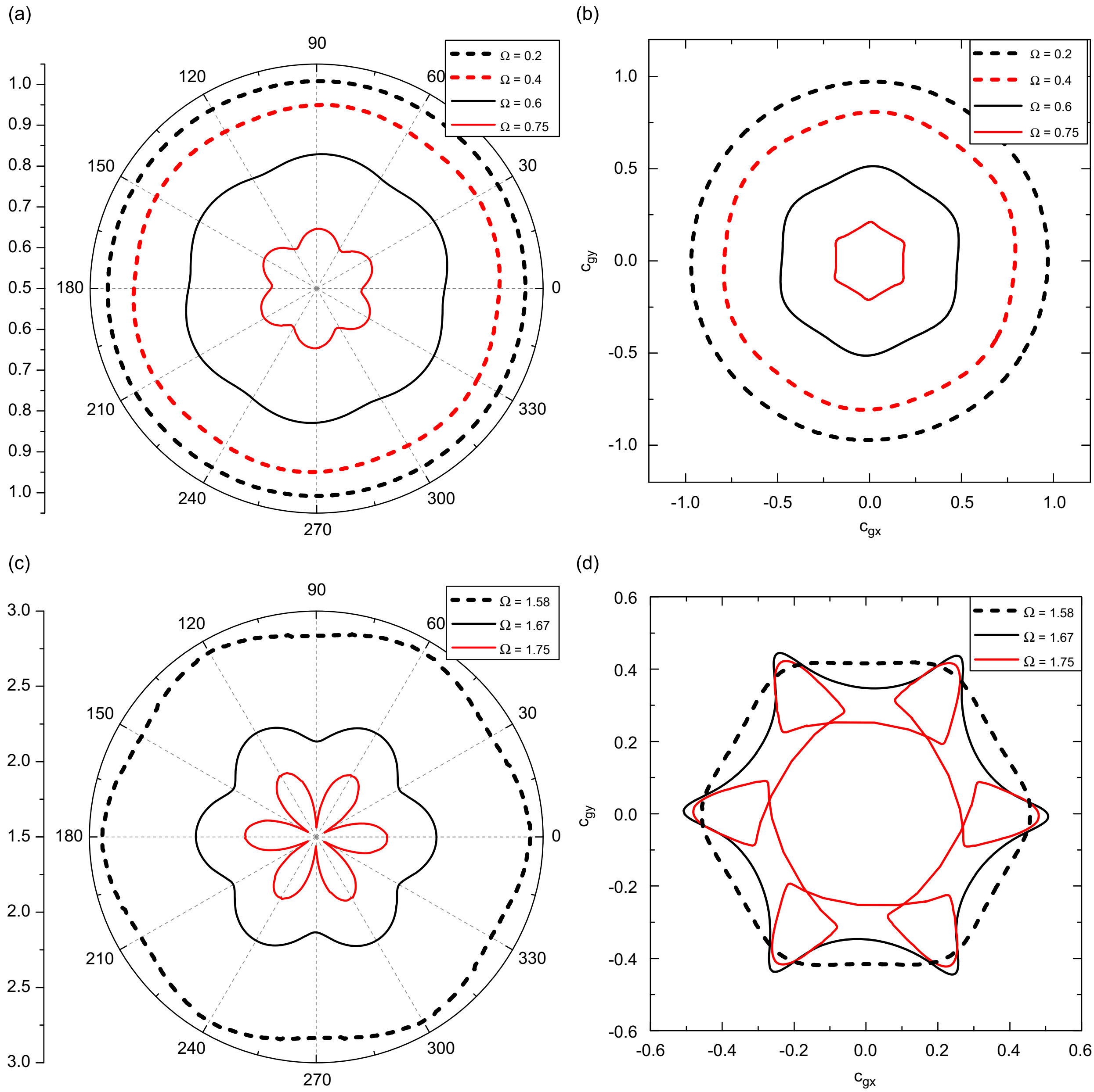

Fig. 11. Phase and group velocities of the first wave mode (a, b) and the fourth wave mode (c, d).

correspondingly, and the remaining parameters are the same as those in Table 2. As L/R decreases with L being unchanged, circles of the chiral lattice become larger (shown in Fig. 13). In the study, core volume fraction of the metamaterial keeps constant. Compared the results in Fig. 5, substantial changes of the wave band structure can be observed. The location of low-frequency bandgaps becomes lower and denser with the decrease of L/R. The appearance of the lower frequency bandgaps is due to the increase of the core mass with the decrease of L/R. The denser low-frequency bandgaps can be explained by the fact that the global stiffness of the structure becomes lower with the increase of r.

Another important factor about the low-frequency bandgaps is the microstructure parameter of the metamaterial inclusion. As we discussed above, the new low-frequency bandgaps are mainly dependent on the local resonant mechanism. The most direct way to tune the resonant frequency is to adjust the core density and the geometry ratio r_c/r. Fig. 14a shows the effects of the normalized core density $\rho_c^* = \rho_c/\rho_c^{\text{ref}}$ upon the normalized low-frequency bandgaps with ρ^{ref} being the density of the metamaterial inclusion core in Table 2. The low-frequency stop bands within $\Omega \in [0,2]$ is represented by red regions. The pass band, which has negative group velocity, corresponds to the white strip. As shown in Fig. 14a, the width of the bandgap increases with the increase of the core density. It is interesting to note that the pass

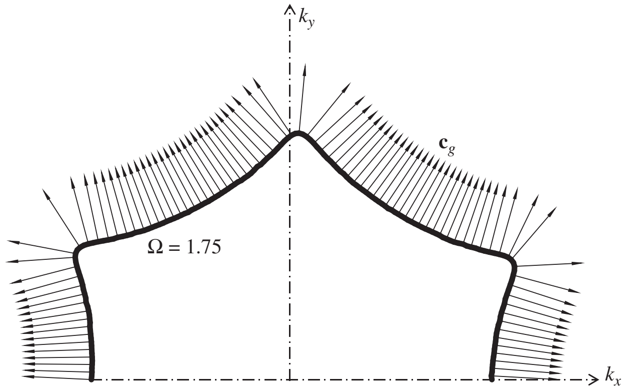

Fig. 12. Caustics stemming from group velocity for the fourth wave mode and $\Omega = 0.83$.

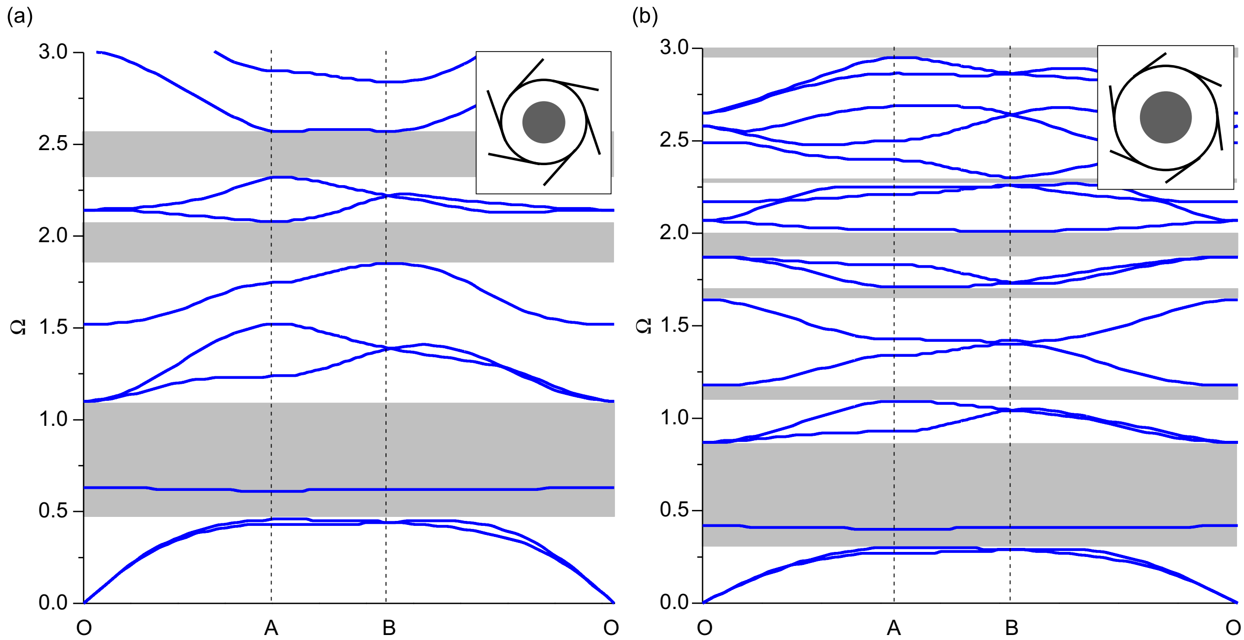

Fig. 13. Band diagram for the topology parameter (a) $L/R = 0.75$ and (b) $L/R = 0.6$.

band, corresponding to the white region in the figure, emerges until $\rho_c^* = 0.5$ and its width decrease with the increase of ρ_c^*. Fig. 14b shows the dependence of the normalized low-frequency bands upon the geometry ratio r_c/r. As shown in the figure, the width of the total bandgap increases with the increase of r_c/r. The pass band can be found until $r_c/r = 0.4$ and its width increases with the increase of r_c/r. These results elucidate how the microstructure parameter of the metamaterial can be used as a tuning parameter for low-frequency bandgaps and the chiral metacomposite can be a good candidate for low-frequency vibration suppression. From this perspective, tuning of the band gap distribution of the chiral metacomposite can be achieved without the need of the change of the overall topology of the chiral lattice.

4.5. *Filtering properties of the finite chiral metacomposite*

In the previous sections, free wave motion characteristics of the infinite chiral metacomposite has been analyzed, however, it may not be suitable for load-carrying application. In this section, a finite metacomposite beam is proposed as shown in Fig. 15. In the beam structure, the periodic chiral metacomposite is sandwiched into a beam frame and the end of the ligament is rigid linked to the frame. The dimension of the beam is W=810 mm in length and H=88 mm in height.

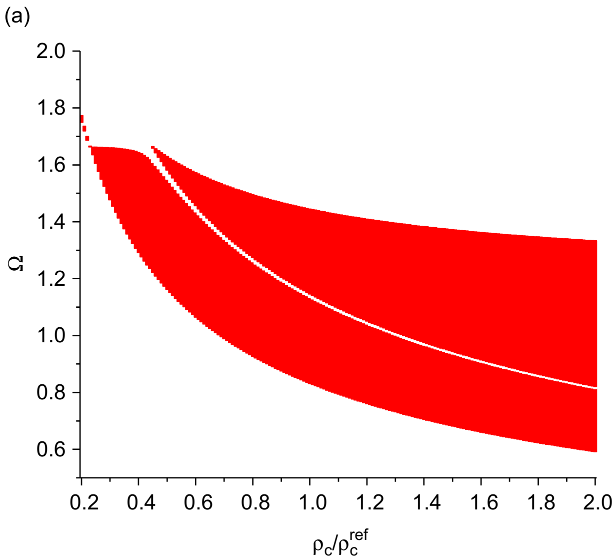

Fig. 14. Bandgap dependence on (a) normalized core density and (b) radius ratio between the core and circle (for interpretation of the references to color in this figure, the reader is referred to the web version of this article).

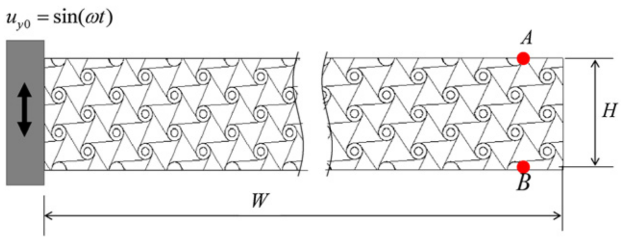

Fig. 15. Geometry and loading conditions of a metacomposite beam.

The material properties of the frame are the same as those of the ligament, and its wall thickness is 1 mm. The structure contains 32 unit cells in length direction and 3 unit cells in height direction. The configuration of the chiral metacomposite is the same as that in Table 2, except for material properties of the metamaterial inclusion. Silicon rubber ($E_s = 3\,\text{MPa}$, $\upsilon_s = 0.48$, $\rho_s = 1.1\,\text{g/cm}^3$) and lead ($E_c = 17\,\text{GPa}$, $\upsilon_c = 0.42$, $\rho_c = 11.3\,\text{g/cm}^3$) are selected as the coating and the core of the metamaterial inclusion, respectively. The beam is free at the right end and the vertical harmonic loading is applied at the left edge of the beam, as shown in Fig. 15. The excitation frequency is swept from 0 to 4000 Hz, corresponding to $\Omega \in [0,2.5]$, to cover a wide range of structural resonances. The response of the beam is characterized by the frequency-response functions (FRF) of the free-tip displacements at points A and B.

Fig. 16a shows calculated response spectra at points A and B of the metacomposite beam. For comparison, response spectra at the same points A and B of a pure chiral lattice beam are also shown in Fig. 16c. Fig. 16b shows the band diagram of the infinite chiral metacomposite, where two stop bands are marked with two gray areas. Significant low transmittance in frequency $\Omega = [0.75,1.15]$ is found for the metacomposite beam, which agrees well with the prediction from the band diagram. However, for the pure lattice beam, the low transmittance cannot be found in the low-frequency range. In relatively high-frequency range, low transmittances are observed in the range $\Omega = [2.25,2.4]$ for both beam structures. The frequency range from the finite beam structure is slightly different from the second bandgap $\Omega = [2.1,2.3]$ predicted from the band diagram, which is based on the infinite periodic structure. This difference may be attributed to the fact that bandgap wave mechanism from the band diagram is the Bragg scattering, which fully relies on the periodicity.

To understand wave mechanism, a deformation snap shot of the metacomposite beam is shown in Fig. 17 at the excitation frequency $\Omega = 0.97$, which is near the middle of the first bandgap. At the frequency, transmittance of the metacomposite beam at the points A and B is less than -21 dB. From the figure, it can be observed that the deformation is localized in the metamaterial inclusion and trapped in the region where the load is applied, and decay very quickly along the length direction. Very small deformation energy is stored in the lattice structure. Since the system is pure elastic and absent of dissipation, the attenuation process in the stop band is very interesting. Through a discrete mass–spring

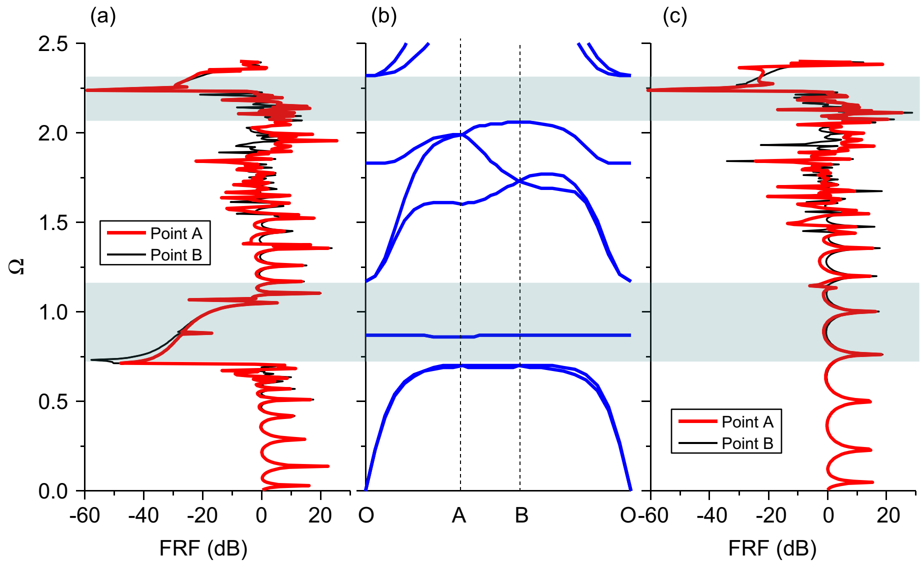

Fig. 16. (a) Frequency spectra of the chiral metacomposite beam, (b) band diagram of the chiral composite and (c) frequency spectra of the pure chiral lattice beam.

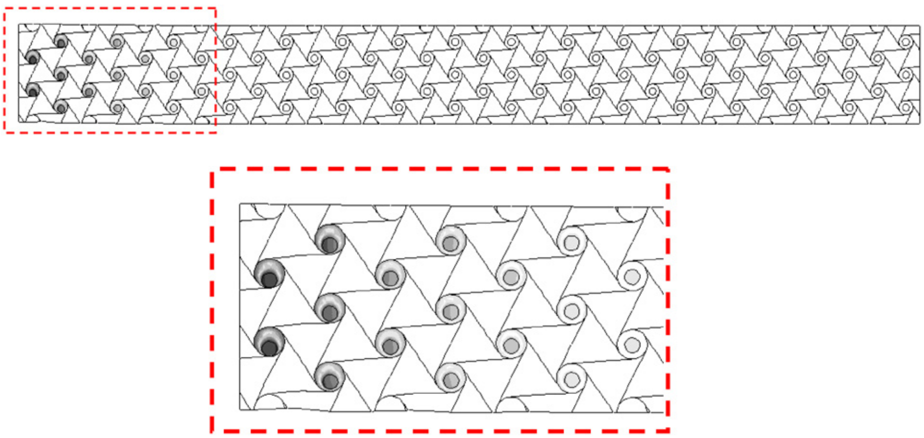

Fig. 17. Deformation of the metacomposite beam under harmonic load at frequency $\Omega = 0.97$.

metamaterial model, Huang and Sun [28] clarified this mechanism through a periodic store-and-return process of the resonance energy in the metamaterial.

To give a deep insight of the spatial attenuation, Fig. 18 shows normalized displacement responses along the top surface of the beam under harmonic loadings with frequencies neighboring the resonant frequency $\Omega_0 = 0.70$ of the metamaterial inclusion. In the figure, the normalized transverse displacement amplitude is defined as $U^* = |u_y|/|u_{y0}|$ with u_y and u_{y0} being the response and excitation displacements, respectively. It is obvious that the displacement response exhibit significant attenuation when the frequency is close to the resonance frequency. The wave will decay totally within two or three unit cells when $\Omega = 1.01\Omega_0$ and decay much slower when the frequency is away from the local resonance frequency.

As we discuss, formation of the low-frequency bandgap in the metacomposite structure is due to the local resonance of the metamaterial inclusion not the Bragg scattering, hence the periodic requirement of the metamaterial inclusion may not be necessary for the low-frequency bandgap. This feature is important since the light weight requirement of a structure is crucial for many engineering application. The proposed metacomposite does not change mechanical properties of the original lattice structure, however, it would result in a considerable weight increase. This non-periodicity feature offers an excellent opportunity to reduce the total weight of the structure by randomly taking off the metamaterial inclusions in the structure. A numerical analysis is conducted on a new metacomposite structure with 50% reduction of the metamateiral inclusion in the metacomposite structure discussed in Fig. 15. Numerical results show that the response spectra of the new metacomposite structure are almost the same as those in Fig. 16. Based on the concept, a boardband vibration suppression can be designed by a chiral metacomposite beam with different types of the metamaterial

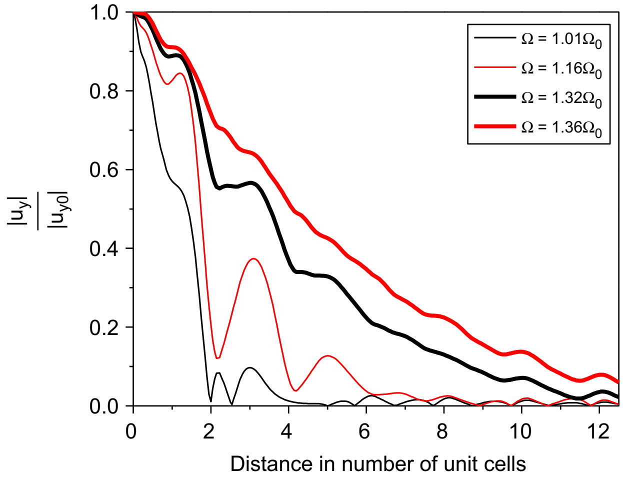

Fig. 18. Spatial attenuation of the displacement response on the surface of the metacomposite beam.

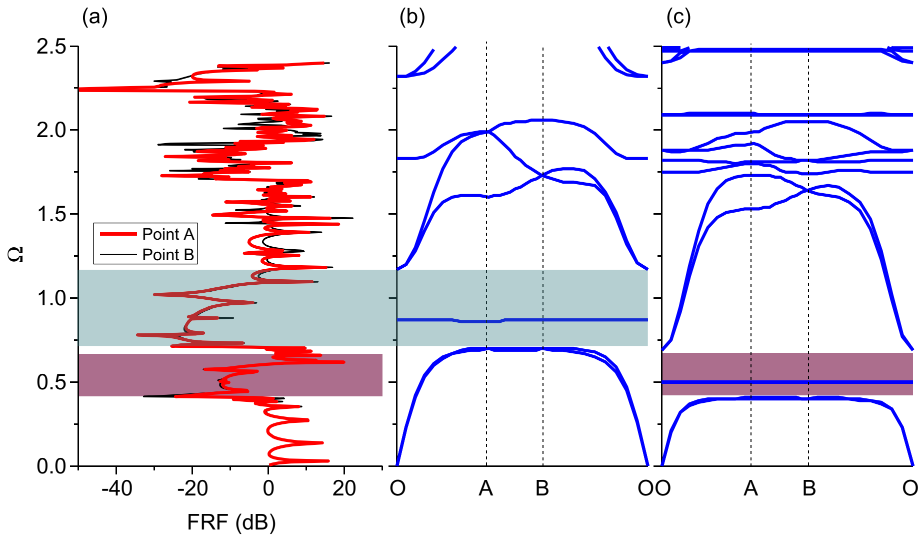

Fig. 19. (a) Frequency response of the metacomposite beam with two metamaterial inclusions; band diagrams of the metacomposite with (b) inclusion A, and (c) inclusion B.

inclusions. In addition to the metamaterial inclusion (inclusion A) used in Fig. 16, another metamaterial inclusion (inclusion B) is also included in the chiral metacomposite beam. The coating's Young's modulus of the new metamaterial inclusion (inclusion B) is changed as $E_s^B = 1\,\text{MPa}$ and the other properties of the metamaterial inclusion B are the same as those of the metamaterial inclusion (inclusion A). Fig. 19a shows the response spectra of the new metacomposite beam with the two metamaterial inclusions (inclusions A and B). In the study, the same beam structure is used as that in Fig. 16 and the metamaterial inclusion A is inserted in the left half of the beam and the metamaterial inclusion B is used in the right half of the beam. For reference, the band diagrams of the metacomposite with the single metamaterial inclusion (inclusion A or B) are shown in Fig. 19b and c, respectively. From the figure, excellent broadband vibration attenuation is achieved in the frequency range =[0.4, 1.2]. Specifically the frequency range is just the sum of that by each individual metamaterial inclusion. This feature will provide a great potential for the design of the broadband vibration suppression.

5. Concluding remarks

In this work, a new chiral metacomposite is suggested by integrating a two-dimensional chiral lattice and a metamaterial inclusion for the low-frequency bandgaps. The matematerial inclusion, which is responsible for the local resonance, composes of a heavy core and a soft coating layer. The in-plane wave propagation in the metacomposite is studied through the finite element technique and Bloch's theorem to illustrate specific wave properties. Effective dynamic properties of the chiral metacomposite are determined to understand wave mechanism of the low-frequency bandgaps in the chiral metacomposite. Tuning of the resulting low-frequency bandgaps is then discussed by adjusting microstructure parameters of the metamaterial inclusion and lattice geometry. Specifically a design of a metacomposite beam structure for broadband low-frequency vibration suppression is demonstrated.

Acknowledgments

This work was supported in part by Air Force Office of Scientific Research under Grant no. AF9550-10-0061 with Program Manager Dr. Byung-Lip (Les) Lee and NSF EAGER program with Program Manager Dr. Lawrence Bank, and in part by National Natural Science Foundation of China under Grant nos. 10972036 and 10832002.

References

[1] A.K. Noor, M.S. Anderson, W.H. Greene, Continuum models for beam-and plate like lattice structures, *AIAA Journal* 16 (1978) 1219–1228.
[2] N. Wicks, J.W. Hutchinson, Optimal truss plates, *International Journal of Solids and Structures* 38 (2001) 5165–5183.
[3] D. Prall, R.S. Lakes, Properties of a chiral honeycomb with a Poisson's ratio—1, *International Journal of Mechanical Sciences* 39 (1996) 305–314.
[4] M.Ruzzene Spadoni, Numerical and experimental analysis of the statice compliance of chiral truss-core airfoils, *Journal of Mechanics of Materials and Structures* 2 (5) (2007) 965–981.
[5] L.J. Gibson, M.F. Ashby, *Cellular Solids: Structure and Properties*, 2nd ed., Cambridge University Press, Cambridge, 1997.
[6] S. Torquato, L.V. Gubiansky, M.J. Silva, L.J. Gibson, Effective mechanical and transport properties of cellular solids, *International Journal of Mechanical Sciences* 40 (1998) 71–82.
[7] R.M. Christensen, Mechanics of cellular and other low density materials, *International Journal of Solids and Structures* 37 (2000) 93–104.
[8] L. Brillouin, *Wave Propagation in Periodic Structures*, Dover, New York, 1953.
[9] R.S. Langley, N.S. Bardell, H.M. Ruivo, The response of two-dimensional periodic structures to harmonic point loading: a theoretical and experimental study of a beam grillage, *Journal of Sound and Vibration* 207 (1997) 521–535.
[10] D. Mead, Wave propagation in continuous periodic structures: research contributions from Southampton 1964–1995, *Journal of Sound and Vibration* 190 (1996) 495–524.
[11] O. Sigmund, J.S. Jensen, Systematic design of photonic bandgap materials and structures by topology optimization, *Proceedings of the Royal Society A* 361 (2003) 1001–1019.
[12] M.I. Hussein, K. Hamza, G. Hulbert, K. Saitou, Optimal synthesis of 2D phononic crystals for broadband frequency isolation, *Waves Random Complex Media* 17 (4) (2007) 491–510.
[13] A.S. Phani, J. Woodhouse, N.A. Fleck, Wave propagation in two-dimensional periodic lattices, *Journal of the Acoustical Society of America* 119 (4) (2006) 1995–2005.
[14] M. Ruzzene, F. Scarpa, F. Soranna, Wave beaming effects in two-dimensional cellular structures, *Smart Materials and Structures* 12 (2003) 363–372.
[15] A. Spadoni, M. Ruzzene, S. Gonella, F. Scarpa, Phononic properties of hexagonal chiral lattices, *Wave Motion* 46 (7) (2009) 435–450.
[16] P.G. Martinsson, A.B. Movchan, Vibrations of lattice structures and phononic bandgaps, *Quarterly Journal of Mechanics and Applied Mathematics* 56 (2003) 45–64.
[17] J.S. Jensen, Phononic band gaps and vibrations in one- and two-dimensional mass–spring structures, *Journal of Sound and Vibration* 266 (2003) 1053–1078.
[18] S. Gonella, A.C. To, W.K. Liu, Interplay between phononic bandgaps and piezoelectric microstructures for energy harvesting, *Journal of the Mechanics and Physics of Solids* 57 (2009) 621–633.
[19] V.G. Veselago, The electrodynamics of substances with simultaneously negative values of ε and μ, *Soviet Physics Uspekhi* 10 (4) (1968) 509–514.
[20] D.R. Smith, W.J. Padilla, D.C. Vier, S.C. Nemat-Nasser, S. Schultz, Composite medium with simultaneously negative permeability and permittivity, *Physical Review Letters* 84 (18) (2000) 4184–4187.
[21] Z.Y. Liu, X.X. Zhang, Y.W. Mao, Y.Y. Zhu, Z.Y. Yang, C.T. Chan, P. Sheng, Locally resonant sonic materials, *Science* 289 (2000) 1734–1736.
[22] Z.Y. Liu, C.T. Chan, P. Sheng, Analytic model of phononic crystals with local resonances, *Physical Review B* 71 (2005) 014103.
[23] J. Li, C.T. Chan, Double-negative acoustic metamateriall, *Physical Review E* 70 (2004) 055602.
[24] J.G. Berryman, Long-wavelength propagation in composite elastic media I. Spherical inclusions, *Journal of the Acoustical Society of America* 68 (1980) 1809–1819.
[25] K.J. Bathe, *Finite Element Procedures*, 1st ed., Prentice-Hall, Upper Saddle River, NJ, 1996.
[26] X.M. Zhou, G.K. Hu, Analytic model of elastic metamaterials with local resonances, *Physical Review B* 79 (2009) 195109.
[27] G.W. Milton, J.R. Willis, On modifications of Newton's second law and linear continuum elastodynamics, *Proceedings of the Royal Society A* 463 (2007) 855–880.
[28] H.H. Huang, C.T. Sun, Wave attenuation mechanism in an acoustic metamaterial with negative effective mass density, *New Journal of Physics* 11 (2009) 013003.